

1 INTRODUCTION

The origins of spotlight-mode synthetic aperture radar (SAR) begin at the Environmental Research Institute of Michigan when Jack Walker developed the theory for range-doppler imaging of moving and rotating objects which we now know as SAR. Walker developed a signal processing technique for radar measurements taken from a target on a rotating plate that overcame previous resolution limits with real aperture imaging radars [1]. The same techniques apply for a moving radar illuminating stationary targets—as is the case with air- and space-borne SAR systems.

Real aperture imaging radars suffer from resolution limits in the cross-range (using a linear FM chirp pulse) given by

$$\rho_x = R\beta = R \frac{\lambda}{D} \quad (1.1)$$

Where R is the standoff distance of the radar to the center of the scene, β is the antenna beamwidth, λ is the radar wavelength and D is the size of the physical antenna aperture. Realistically, choice of R is limited by the platform choice for the radar system and application, and the antenna beamwidth is limited by antenna size and choice of frequency—which ideally is chosen such that the pulse has little to no attenuation through Earth's atmosphere) [2]. As we will see, SAR overcomes this limit and becomes *inversely* proportional to the size of the synthetic aperture. The range resolution remains the same for real and synthetic aperture radars since the same processing is used for ranging.

Radar measurements can be expressed as integrals of the reflectivity function of the ground patch being illuminated. Walker proposed taking radar measurements at multiple locations and storing them in a polar format than can be related to the Fourier transform of the ground reflectivity. With enough samples, an inverse Fourier transform can be taken of the samples to reconstruct an estimate of the ground reflectivity. Today, this algorithm is commonly referred to as the polar format algorithm (PFA) [1].

Preceding this work by Walker, engineers in medical imaging developed the technology for computer axial tomography (CAT) for x-ray scanning (and subsequently almost all modern medical imaging techniques). Before the invention of the CAT scan, x-rays were taken as a profile of the imaging medium and the image formed was the accumulation of all attenuation along the path of the x-rays traveling through the entire medium. Hounsfield developed CAT which consisted of an x-ray source and detector rotating around the medium to be imaged taking measurements through 180° of rotation. These measurements were projections of the attenuation function of the medium. These projections are directly related to the 2D Fourier transform of the attenuation function and thus by measuring many of these projections, a portion of the spatial frequency spectrum of the

attenuation function of the medium is sampled. The reconstructed image of the medium is simply the inverse discrete Fourier transform of the projection data placed on a polar grid [3] [2].

What Hounsfield's work did for SAR was provide a generalized signal processing description of a very similar technology in the field of medical imaging. The connection was made to Walker's work and published by Munson et al. in 1983. This new description of SAR utilized the so-called projection-slice theorem (the backbone of CAT theory) to describe the relationship between SAR measurements and the reflectivity function of the illuminated terrain. Through this work SAR imaging is viewed as a narrow-band version of CAT imaging because CAT scans over 180° while SAR might scan over only a few degrees thus sampling a smaller portion of the spatial frequency spectrum of the reflectivity (or attenuation in the case of CAT) function. Additionally, Walker utilized radar specific jargon to describe SAR so Munson's paper opened understanding of the subject to those outside the radar community [4].

Munson et al.'s work also extended understanding of SAR processing to utilize methods from CAT like the convolution backprojection (CBP) algorithm for image formation. Convolution backprojection has shown improvement in image quality and can process the SAR measurements as they are obtained whereas PFA must wait until all measurements are collected to begin processing. The drawback of CBP is its computational inefficiency compared to PFA [4]. Reconstructing an $N \times N$ image using PFA scales as $O(N^2 \log N)$ whereas CBP scales as $O(N^3)$ [5]. PFA and CBP are still widely used algorithms in production level SAR systems and claims to CBP's image quality improvements have been refuted in more recent studies [6].

The following topic of discussion will be the polar format algorithm followed by a simple simulation demonstrating use of the algorithm. The terminology and derivations will utilize the CAT-based formulation detailed by Munson et al with additional detail added from Jakowatz's textbook [2] [4].

2 BACKGROUND

Consider the SAR imaging geometry described in Figure 1. The SAR is airborne and flying on a straight flight path illuminating a scene on the ground. The center of the illuminated scene is the origin of the standard cartesian coordinate system and the line connecting the radar to the origin is described by polar coordinates (θ, ψ) . θ is often referred to as the azimuth angle and ψ as the depression or elevation angle. A rotated coordinate system described by (u, v, w) is defined relative to the position of the radar to the origin. The illuminated scene is the circle of radius L centered at the origin and the distance from the origin to the radar is R .

Consider the transmitted radar signal known as a linear frequency modulated (FM) chirp given by

$$s(t) = \begin{cases} \exp[j(\omega_0 t + \alpha t^2)], & \forall t \in \left[-\frac{T}{2}, \frac{T}{2}\right] \\ 0, & \text{otherwise} \end{cases} \quad (2.1)$$

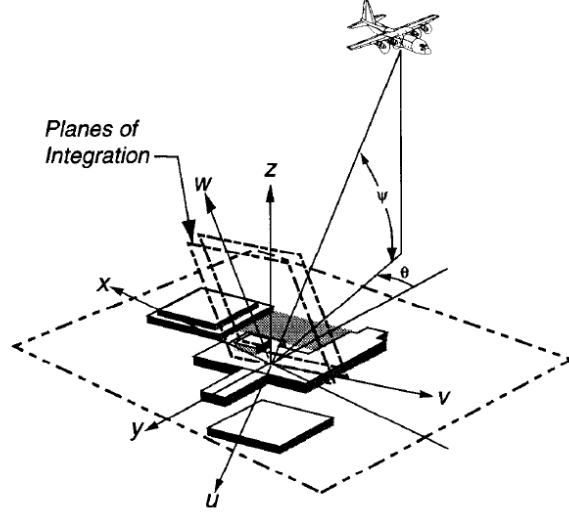


Figure 1: Geometry of the SAR system used throughout the PFA derivation [2].

Where ω_0 is the center frequency of the pulse, 2α is the chirp rate and T is the pulse duration. The bandwidth of the linear FM chirp is $B_c = \frac{\alpha T}{\pi}$ Hz. The goal is to measure the reflection of $s(t)$ from many positions with the radar and process those measurements to reconstruct an image of the area illuminated by the radar. The transmitted signal reflects off the illuminated scene we wish to reconstruct an image of according to the reflectivity function given by $g(x, y, z)$ such that

$$r_{\theta,\psi}(t) = |g(x, y, z)|s(t)e^{j\angle g(x,y,z)}$$

is the returned signal when measured from position (R, θ, ψ) . Since radars operate at frequencies with effectively no attenuation through the atmosphere, we can assume all attenuation is due to the reflectivity of the surface. Note that $g(x, y, z)$ is zero everywhere except on a two-dimensional subspace and is, in general, complex valued. To simplify our analysis, we will assume $g(x, y, z) = 0 \forall z \neq 0$, but in practice doing this will introduce distortions in the final image.

Radar images can be broken into two dimensions: range and cross-range. Range is the direction in line with the radar beam in the ground plane and cross-range is the direction orthogonal to the range in the ground plane and it is parallel to the flight path (assuming a straight flight path). These correspond to the y and x directions, respectively, when $\theta = 0$.

3 RESOLVING THE RANGE

Resolving the range dimension is the first step to estimating an image of the ground reflectivity and is done in the same way it is for real aperture radars.

First, if the transmitted signal is $s(t)$ given by equation (2.1), then the signal returned to the radar after scattering off the illumination zone is

$$r_{\theta,\psi}(t) = A \operatorname{Re} \left\{ \int_{-u_1}^{u_1} p_{\theta,\psi}(u) s \left(t - \frac{2(R+u)}{c} \right) du \right\} \quad (3.1)$$

Where A is a scale factor, R is the distance from the radar to the center of the illuminated scene and c is the speed of light. u is called the slant range and is related to the range by

$$u = y \cos \psi \quad (3.2)$$

and u_1 is the corresponding radius of the illuminated scene in slant range. $p_{\theta,\psi}(u)$ is the projection function and is given by

$$p_{\theta,\psi}(u) = \int_{-\infty}^{\infty} \int_{-\infty}^{\infty} g[x(u, v, w), y(u, v, w), z(u, v, w)] dv dw \quad (3.3)$$

This can be interpreted by noting that v and w form a plane orthogonal to the slant range direction which is the direction the pulse travels along. Since the scene lies in the far-field of the radar, the wavefronts are approximately planar and aligned with the plane formed by v and w . This means that reflections from all points in a plane in v and w will reflect and be received at the radar at the same time. This culminates in the returned signal being the convolution of the transmitted signal with the reflectivity function integrated over all v and w as shown in equation (3.1). Note that this far-field approximation does not always hold and can create distortions in the final image.

If we can deconvolve $p_{\theta,\psi}(u)$ from $s(t)$, then we have distinguished all targets along the range dimension. This deconvolution is done via deramp processing. Deramp processing first mixes (multiplies) the returned signal by in-phase and quadrature local versions of the transmitted pulse separately. These in-phase and quadrature terms are respectively

$$s_i(t) = \cos\left(\omega_0\left(t - \frac{2R}{c}\right) + \alpha\left(t - \frac{2R}{c}\right)^2\right) \quad (3.4)$$

$$s_q(t) = \sin\left(\omega_0\left(t - \frac{2R}{c}\right) + \alpha\left(t - \frac{2R}{c}\right)^2\right) \quad (3.5)$$

We then construct a complex signal from the two mixing operations

$$\tilde{r}_{\theta,\psi}(t) = r_{\theta,\psi}(t)s_i(t) + jr_{\theta,\psi}(t)s_q(t) \quad (3.6)$$

We then low pass filter the complex signal given by equation (3.6) to get the deramped return signal

$$\bar{r}_{\theta,\psi}(t) = \frac{A}{2} \int_{-u_1}^{u_1} p_{\theta,\psi}(u) \exp\left(j\left[\alpha\left(\frac{2u}{c}\right)^2 - \frac{2u}{c}\left(\omega_0 + 2\alpha\left(t - \frac{2R}{c}\right)\right)\right]\right) du \quad (3.7)$$

The quadratic phase term $\alpha\left(\frac{2u}{c}\right)^2$ can be handled in one of two ways. One is to inverse Fourier transform equation (3.7), multiply by $\exp\left(-j\alpha\left(\frac{2u}{c}\right)^2\right)$ to remove the term, then transform back. This introduces error because we don't know $\bar{r}_{\theta,\psi}(t)$ for all t and thus are not going to compute the true inverse transform. The second option is to leave the quadratic phase term if it is small enough and accept a small penalty to resolution in the final SAR image. Generally, if

$$\frac{4\alpha L^2}{c^2} \ll \frac{\pi}{2}$$

then the loss of resolution is small. For this analysis we simply ignore the quadratic phase term and $\bar{r}_{\theta,\psi}(t)$ becomes

$$\bar{r}_{\theta,\psi}(t) = \frac{A}{2} \int_{-u_1}^{u_1} p_{\theta,\psi}(u) \exp\left(-j \frac{2u}{c} \left(\omega_0 + 2\alpha \left(t - \frac{2R}{c}\right)\right)\right) du \quad (3.8)$$

Note how this resembles a Fourier transformation if we let

$$U = \frac{2}{c} \left(\omega_0 + 2\alpha \left(t - \frac{2R}{c}\right)\right)$$

Then

$$\bar{r}_{\theta,\psi}(t) = \frac{A}{2} \int_{-u_1}^{u_1} p_{\theta,\psi}(u) \exp(-jUu) du = \frac{A}{2} P_{\theta,\psi}(U) \quad (3.9)$$

Where

$$\frac{2}{c}(\omega_0 - \pi B_c) \leq U \leq \frac{2}{c}(\omega_0 + \pi B_c) \quad (3.10)$$

Equations (3.9) and (3.10) reveal that by taking the inverse Fourier transform along the slant range direction U of the deramped return signal, then the range direction of the image has successfully been reconstructed, however, we also need to distinguish targets in the cross-range direction which so far has not been accomplished with this algorithm. With this function alone, two targets with the same range and different cross-ranges will be indistinguishable.

4 RESOLVING CROSS-RANGE

To resolve cross-range the radar takes measurements along its flight path so that many projection functions, $P_{\theta,\psi}(U)$, are obtained for a variety of θ and ψ values since U is defined relative to the radar's position. The projection-slice theorem can then be applied to relate the projection functions to the spatial frequency spectrum (also known as the phase history domain) of the reflectivity function.

Consider the projection function for $(\theta, \psi) = (0,0)$ given by

$$p_{0,0}(x) = \int_{-\infty}^{\infty} \int_{-\infty}^{\infty} g(x, y, z) dy dz \quad (4.1)$$

And its Fourier transform given by

$$P_{0,0}(X) = \int_{-\infty}^{\infty} \int_{-\infty}^{\infty} \int_{-\infty}^{\infty} g(x, y, z) e^{-jXx} dx dy dz \quad (4.2)$$

If we take the Fourier transform of $g(x, y, z)$ and evaluate it for polar coordinates $(\theta, \psi) = (0,0)$ we get

$$\begin{aligned}
G(X, 0, 0) &= \int_{-\infty}^{\infty} \int_{-\infty}^{\infty} \int_{-\infty}^{\infty} g(x, y, z) e^{-jXx} e^{-j(0)y} e^{-j(0)z} dx dy dz \\
&= \int_{-\infty}^{\infty} \int_{-\infty}^{\infty} \int_{-\infty}^{\infty} g(x, y, z) e^{-jXx} dx dy dz \\
&= P_{0,0}(X)
\end{aligned} \tag{4.3}$$

Thus it has been shown that the Fourier transform of the projection function when $(\theta, \psi) = (0, 0)$ is equal to the Fourier transform of the reflectivity function when $(\theta, \psi) = (0, 0)$. It is well known that a rotation of an arbitrary function results in an equivalent rotation to that function's Fourier transform. Therefore, we can extend equation (4.3) to state that the Fourier transform of the projection function along U for any given θ and ψ is equal to a line oriented according to angles θ and ψ of the Fourier transform of the ground reflectivity function. Mathematically speaking

$$P_{\theta,\psi}(U) = G(X, Y, Z) \tag{4.4}$$

This is known as the projection-slice theorem and is the basis of measuring cross-range of targets. If we measure many projection functions, then we can populate a portion of the phase history domain of the reflectivity function, then take the 2D inverse Fourier transform of the phase history domain samples to reconstruct an image of the illuminated scene. All that is required to measure many projection functions is to vary θ and ψ by moving the radar along its flight path. Ultimately, our data will span an annulus in the phase history domain and the samples will have a polar distribution on the annulus as shown in Figure 2. The top raster are the samples on the annulus as measured by the SAR. The samples on the bottom annulus are ground projected. Projecting the samples to the ground plane prior to image formation is desirable because there is range distortion that occurs if the image is formed in the slant plane due to the difference in the grazing angle for targets closest to the radar compared to targets farthest from the radar [7]. This distortion may be negligible if $R \gg L$ so it becomes problem dependent as to whether ground projection should be done.

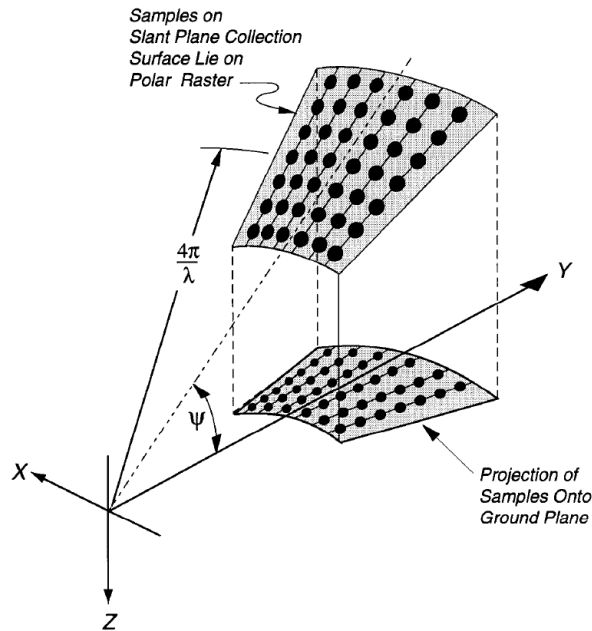


Figure 2: Depiction of polar raster of data samples in the phase history domain. The top annulus is the data as measured in the slant plane and the bottom annulus is the measured data after being projected to the ground plane [2].

Whether or not the data samples are projected to the ground plane, the samples are then interpolated to a cartesian grid. While this step is actually unnecessary for computing an inverse discrete Fourier transform (DFT) of the samples, it enables the use of the fast Fourier transform (FFT) algorithm in computing the DFT. After interpolation, it is common to window the samples to reduce sidelobe levels. The spatial frequency offset from the center of the annulus to the origin is equal to $\frac{4\pi}{\lambda}$ which is proportional to the center frequency of the transmitted radar signal. This offset is removed so that the center of the annulus is at the origin prior to inversion of the transform.

Finally, the samples can be inverse Fourier transformed to obtain the estimate of the ground reflectivity

$$\hat{g}(x, y, z) = \mathcal{F}^{-1}\{G(X, Y, Z)\} \quad (4.5)$$

5 PERFORMANCE

SAR is touted for overcoming the cross-range resolution limit imposed in equation (1.1) and with a little further analysis we can show this to be true. We begin with a determination of the bandwidth of $G(X, Y, Z)$ by considering the samples in the slant plane. From our previous analysis, we showed the spatial frequency along the range is bounded in equation (3.10) therefore the bandwidth along the slant range direction is given by

$$\Delta U = \frac{2}{c}(2\pi B_c) \quad (5.1)$$

The bandwidth along the cross-range dimension is calculated from the distance to the annulus center from the origin and the angular extent, $\Delta\theta$, of the annulus as determined by the flight path.

$$\Delta X = \frac{4\pi}{\lambda} \Delta\theta \quad (5.2)$$

The spatial resolutions follow from the bandwidths directly. The slant range resolution is given by

$$\rho_u = \frac{2\pi}{\Delta U} = \frac{c}{2B_c} \quad (5.3)$$

And the cross-range resolution is given by

$$\rho_x = \frac{2\pi}{\Delta X} = \frac{\lambda}{2\Delta\theta} \quad (5.4)$$

Now we have confirmed that the cross-range resolution is inversely proportional to $\Delta\theta$ which is increased by having a longer flight path (i.e. longer synthetic aperture). Similarly, we can quantify the resolution of a ground projected image though there are additional considerations based on the geometry of the imaging mode. Imaging modes can be classified as broadside or squint modes. Broadside imaging is when the range direction is orthogonal to the flight path and squint modes are all the rest. When the data samples are ground projected in a squint, there is skewing of the data annulus and this case will not be analyzed here. In a broadside collection, the data annulus is only

contracted along the range direction in ground projection according to the relationship between the slant range and range given by equation (3.2) therefore the range resolution is given by

$$\rho_y = \frac{2\pi}{\Delta Y} = \frac{c}{2B_c \cos \psi} \quad (5.5)$$

The cross-range resolution stays the same as in a slant plane image given by equation (5.4). Do not be too quick to draw the conclusion that the image formed in the slant plane somehow has better resolution based on equations (5.3) and (5.4). Although the resolution will be higher in the slant plane image, the targets are also proportionally closer together therefore the image will not actually reveal more information.

6 SIMULATION

To demonstrate the functionality of the PFA algorithm, let us consider a paired down example from the previous derivation. We will now assume that the SAR exists in a 2D world as shown in **Error! Reference source not found.** and the antenna has a uniform radiation pattern that has unity gain in the illuminated footprint region circumscribed by the circle of radius L centered at the origin and has zero gain elsewhere. The collection type is broadside and the radar flies along a circular arc

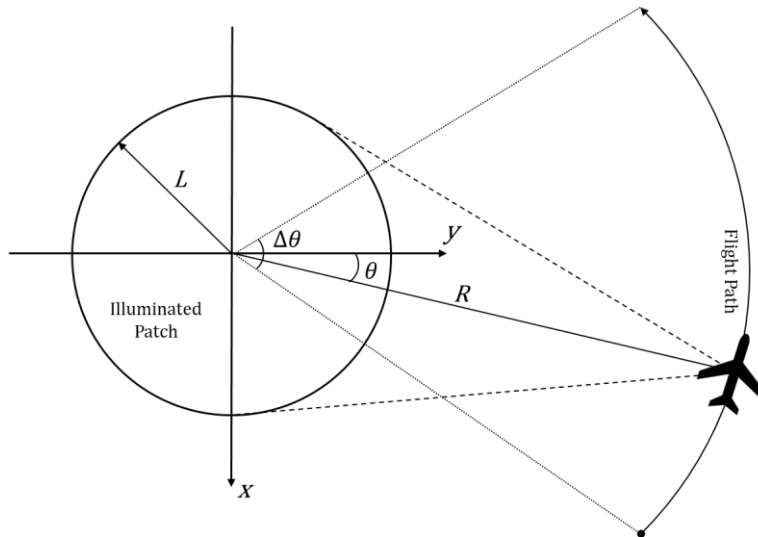


Figure 3: The geometry used to describe the SAR simulation.

spanning angle $\Delta\theta$.

The same linear FM chirp given by equation (2.1) is used as the transmitted radar signal and the return signal follows from equations (3.1) and (3.3)

$$r_\theta(t) = A \operatorname{Re} \left\{ \int_{-L}^L p_\theta(y) s \left(t - \frac{2(R+y)}{c} \right) dy \right\} \quad (6.1)$$

Where

$$p_\theta(y) = \int_{-L}^L g(x, y) dx \quad (6.2)$$

The return signal, $r_\theta(t)$, is assumed to undergo deramp processing with a hardware implementation. This is commonly done because lower sampling rates are required in analog-to-digital conversion of the deramped signal compared to the raw return signal due to the lower center frequency of the deramped signal [2]. The deramped signal is given by

$$\bar{r}_{\theta, \psi}(t) = \frac{A}{2} \int_{-L}^L p_\theta(y) \exp\left(-j \frac{2y}{c} \left(\omega_0 + 2\alpha \left(t - \frac{2R}{c}\right)\right)\right) dy = \frac{A}{2} P_\theta(Y) \quad (6.3)$$

The simulation starts by computing equation (6.3) using simple rectangular approximations to the integrals and ensuring the sampling rate is high enough to avoid aliasing. This is repeated for each location along the simulated flight path we take measurements at. These measurements are polar formatted samples of the phase history and must be interpolated to a cartesian grid to be amenable to the FFT algorithm.

Figure 4 shows this polar raster formatted data and a box outlining the region interpolated within. Using a region completely contained in the annulus spanned by the phase history samples is important to avoid extrapolating the data which if not done carefully would lead to erroneous results. Lastly, the samples are inverse Fourier transformed to obtain the estimated reflectivity of the ground patch being illuminated.

Figure 4: A polar raster of phase history samples with a box overlaid within which the samples are interpolated to a cartesian grid.

A key consideration in implementing such a simulation is the sampling rate used for various parts of this algorithm. The first signal sampled is the ground reflectivity function along x . For this, we only need enough samples to well approximate the integration along x that is done in equation (6.2). The next signal we need to sample is the projection function, $p_\theta(y)$, which must abide by the Nyquist-Shannon sampling theorem. We know the spatial bandwidth of $p_\theta(y)$ from equation (3.10) therefore the maximum spatial frequency is

$$Y_{max} = \frac{2}{c}(\omega_0 + \pi B_c)$$

And the minimum sampling frequency of y is twice the maximum spatial frequency of y .

$$f_y = 2Y_{max} \quad (6.4)$$

Similarly, the sampling rate in time for the deramped signal is computed based on the maximum temporal frequency in the signal which we can directly determine from equation (6.3) and noting that the maximum time is $t = \frac{2R}{c} + \frac{T}{2}$ and $\alpha = \frac{\pi c}{2\rho_y T}$ then

$$\omega_{max} = \frac{4y_{max}\alpha}{c} = \frac{2\pi y_{max}}{\rho_y T}$$

Therefore the minimum sampling frequency in time is

$$f_t = \frac{2y_{max}}{\rho_y T} \quad (6.5)$$

In this simulation, the models for ground reflectivity are defined as N circular patches with a reflectivity of 1 and 0 everywhere else. Mathematically, it is expressed as

$$g(x, y) = \sum_{i=1}^N a_i g_i(x, y, x_i, y_i, r_i) \quad (6.6)$$

where

$$g_i(x, y, x_i, y_i, r_i) = \begin{cases} 1, & \sqrt{(x - x_i)^2 + (y - y_i)^2} \leq r_i \\ 0, & \text{otherwise} \end{cases}$$

Where a_i is a scale factor, r_i is the radius of the i^{th} reflective circle and x_i and y_i are arbitrary shifts along x and y , respectively, and N is the number of circular targets in the patch.

Consider an example where $R = 1$ km, $L = 10$ m, $f = 299.792458$ MHz. Choice of these parameters was primarily motivated by ease to simulate and derive a consistent set of parameters. If we want a desired range and cross-range resolution of $\rho_x = \rho_y = 1$ m, then we can compute the angular extent of the flight path and pulse parameters with equations (5.4) and (5.5). Using these parameters, three different ground reflectivities were illuminated and estimations of them using the polar formatting algorithm were created. The true reflectivities with a high resolution are shown in the top row images of Figure 5 **Error! Reference source not found.** and the corresponding estimated reflectivities are shown in 20x20 pixel images in the bottom row. The desired resolution of 1m over an illuminated patch with a radius of 10m means any more than 20 pixels along x and y is redundant. There are three cases shown:

- a) There is a single reflector of radius 2.5 m centered at $(x, y) = (0, 0)$ with a reflectivity of 1. The corresponding estimated reflectivity does represent the presence of a strong reflector near the origin; however, there is a splitting of the target going on as evident by the lack of reflectivity where the center of the target should be.

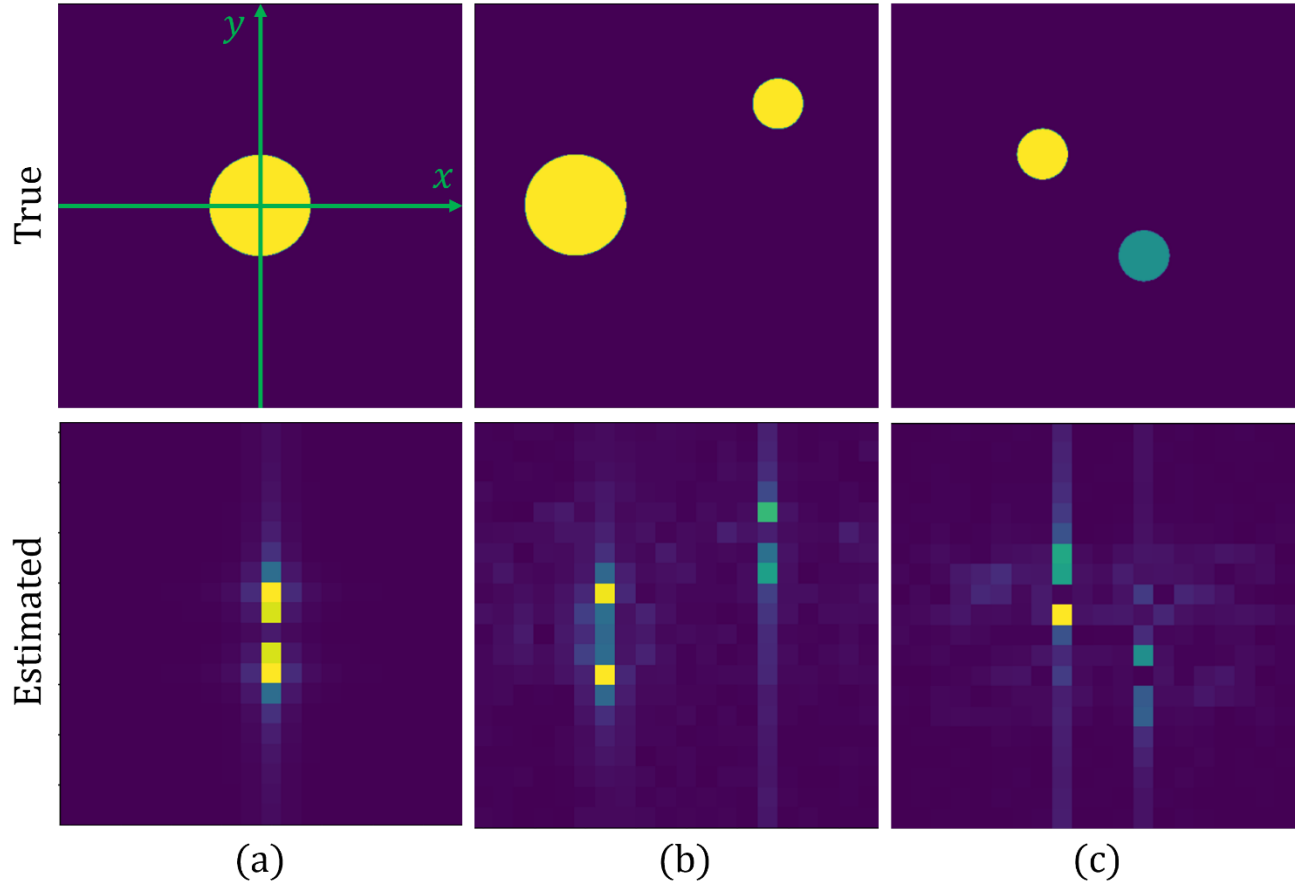


Figure 5: The top row images are of three true ground reflectivities that we simulate measurements of. The bottom row shows the estimated ground reflectivities from applying the polar format algorithm to the simulated radar measurements.

- b) There are two reflectors—both with a reflectivity of 1. The large reflector is shifted along x by -5 m with a radius of 2.5 m and the second reflector is shifted along x and y by 5 m with a radius of 1.25 m. As with case one, it is clear there are strong reflectors at the corresponding locations in the estimated reflectivity, but the splitting effect is still present. Additionally, the smaller target appears weaker than the larger target despite it having the same true reflectivity.
- c) The reflectivity contains two reflectors. The first reflector is shifted along x and y by -2.5 m and 2.5 m, respectively, with a radius of 1.25 m and reflectivity of 1. The second reflector is shifted along x and y by 2.5 m and -2.5 m, respectively, with a radius of 1.25 m and reflectivity of 0.5. Both targets are distinguishable and the difference in reflectivity is noticeable as well, but the splitting effect is still present.

While all the targets are distinguishable, there are a few unwanted effects in the SAR images. The first being the splitting effect in which a target appears to be split into two smaller targets. The two smaller targets are generally only one or two pixels in width and/or height and their separation is approximately twice the radius of the true target. I attempted to replicate the inverse of example a in Figure 5 to further investigate this effect. I used a true reflectivity mimicking the estimated reflectivity in example a and hoped to produce an estimated reflectivity like the true reflectivity of example a. As shown in Figure 6, this did not succeed and there appears to be additional splitting now occurring along the cross-range (y) direction.

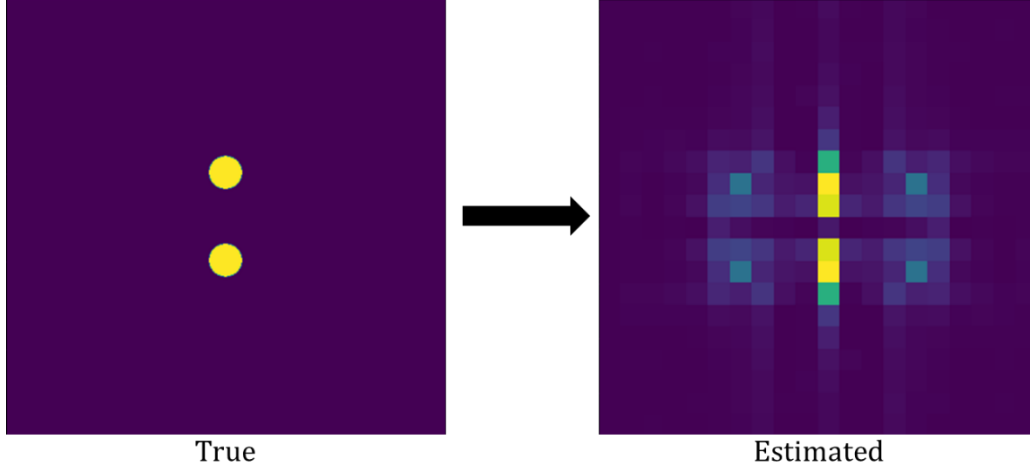


Figure 6: Simulating the inverse of example a in Figure 5 as an attempt to invert the splitting effect.

The second concerning effect in the estimated reflectivities is that they are complex valued such that order of the real and imaginary parts are, in general, comparable to each other meaning this is not just due to numerical artifacts in the results. The true reflectivities were real-valued so I expect the estimated reflectivities to be approximately real-valued as well. It is possible this can be explained by the complex exponential that shows up due to the narrowband approximation of the phase history as shown later in equation (6.7).

The last point of concern is in the magnitude of the estimated reflectivities. Since this simulation is not concerned with physical losses beyond reflectivity, I would expect each estimated reflectivity to have a magnitude of half of the corresponding true reflectivity due to equations (3.9) and (4.4). I am observing magnitudes between one and two orders of magnitude less than the true reflectivity. Note that the upcoming discussion on smoothing effects does not account for this magnitude change.

The difficulty in finding the sources of these issues and resolving them comes from my relatively limited knowledge of SAR (hence why this project is a review of one of the fundamental algorithms used in SAR image formation). It is difficult to determine what effects *should* be present and which are due to errors in the simulation without an intimate knowledge of SAR algorithms and image phenomenology. Subsequently, it is also a challenge to back propagate the unwanted effects (such as the target splitting) through the polar format algorithm to determine what might be its cause.

An explainable and expected effect in the estimated reflectivities are the strong lines of reflectivity protruding outwards along the y direction and sometimes x direction from the targets. These lines are due to the narrowband approximation intrinsic to the numerical nature of image formation. Since we can only sample a finite interval of the return signal, we are only sampling a finite portion of the phase history. Mathematically we are effectively taking samples of

$$\Pi\left(\frac{Y - \frac{2\omega_0}{c}}{\frac{4\pi B_c}{c}}\right) \frac{A}{2} P_\theta(Y)$$

as opposed to the entirety of $\frac{A}{2}P_\theta(Y)$ where $\Pi(Y)$ is the rectangle function. Taking the inverse Fourier transform of this turns the multiplication into a convolution (denoted by \otimes) in the spatial domain.

$$\mathcal{F}^{-1}\left\{\Pi\left(\frac{Y - \frac{2\omega_0}{c}}{\frac{4\pi B_c}{c}}\right)\frac{A}{2}P_\theta(Y)\right\} = \frac{A}{2}\hat{g}(x, y) \otimes \frac{4\pi B_c}{c}e^{-j4\pi\frac{\omega_0}{c}y}\text{sinc}\left(\frac{4\pi B_c}{c}y\right) \quad (6.7)$$

Convolution with a sinc function along y creates a smoothing effect along the same direction. This is apparent in the estimated images as the lines of strong reflectivity decaying outward of each target along the y direction. Since we are also sampling along X , this effect will manifest itself along the x direction in the estimated reflectivities all the same. In the examples in Figure 5 the effect along y is much more apparent than along x and it is still an open question, for me, as to why this is the case. If we were able to sample the entire phase history along Y , then the rectangle function would become infinite in extent and its inverse Fourier transform would be a delta function thus having no smoothing effect.

Overall, this project provided an introduction to the motivation for SAR, a detailed explanation of the polar format algorithm for forming SAR images and the results of a simple 2D simulation utilizing the PFA to form a SAR image. There are some questionable effects such as the splitting of the targets in the results, but the fact that targets are distinguishable and there are quantifiable effects such as the smoothing effect present in the estimated reflectivities makes this simulation a success.

References

- [1] J. L. Walker, "Range-Doppler Imaging of Rotating Objects," *IEEE Transactions on Aerospace and Electronic Systems*, Vols. AES-16, no. 1, pp. 23-52, 1980.
- [2] C. V. Jakowatz, *Spotlight-mode Synthetic Aperture Radar: A Signal Processing Approach*, Springer Science+Business Media, 1996.
- [3] G. N. Hounsfield, "Computerized transverse axial scanning (tomography) Part I. Description of system," *British Journal of Radiology*, vol. 46, no. 552, pp. 1016-1022, 1973.
- [4] D. Munson, J. O'Brien and W. Jenkins, "A tomographic formulation of spotlight-mode synthetic aperture radar," *Proceedings of the IEEE*, vol. 71, no. 8, pp. 917-925, 1983.
- [5] M. Desai and W. Jenkins, "Convolution backprojection image reconstruction for spotlight mode synthetic aperture radar," *IEEE Transactions on Image Processing*, vol. 1, no. 4, pp. 505-517, 1992.
- [6] C. V. Jakowats and N. Doren, "Comparison of polar formatting and back-projection algorithms for spotlight-mode SAR image formation," *SPIE Proceedings*, vol. 6237, 2006.
- [7] A. Doerry, *SAR Phenomenology*, 2017.